V. 1. Progress of The Tohoku Microbeam System

Matsuyama S.[1], Ishii K.[1], Yamazaki H.[1], Kikuchi Y.[1], Inomata K.[1], Watanabe Y.[1], Ishizaki A.[1], Oyama R.[1], Kawamura Y.[1], Yamaguchi T.[1], Momose G.[1], Nagakura M.[1], Takahashi M.[1], and Kamiya T.[2]

[1]*Department of Quantum Science and Energy Engineering, Tohoku University*
[2]*Takasaki Advanced Radiation Research Institute, Japan Atomic Energy Agency*

Introduction

High-energy ion microbeams are powerful analytical tools that combine various ion beam analysis techniques such as PIXE, RBS, STIM, and SEM[1-3]. They are also attractive as a direct lithographic technique. We have developed a microbeam analysis system for biological applications with sub-micrometer resolution. The primary purpose was to develop a 3D μ-CT, in which a microbeam is used as a monoenergetic point X-ray source. The second was to develop a microbeam analysis system for biological samples. The microbeam line was installed in July 2002; the system produced a beam spot size of 2×2 μm^2 with a beam current of 10 pA. Both the beam size and beam current were insufficient for ion beam analyses. Optimization and modification of the system were performed and the analysis system was re-developed. After optimization and modification of the system, the beam performance was remarkably improved and a multimodal analysis system was developed. This paper presents a description of recent progress of the microbeam system.

Microbeam System

The microbeam system was designed to achieve sub-micrometer beam sizes and was developed in collaboration with Tokin Machinery Corp[4]. The system is connected to the 4.5 MV Dynamitron accelerator at Tohoku University. A high-resolution energy analysis system is installed upstream of the microbeam line to confine the energy variation so as to achieve sub-micrometer beam sizes. The microbeam line comprises a quadrupole doublet and three slit systems: micro-slit (MS), divergence-defining slit (DS), and baffle slit (BS). These components are mounted on a heavy rigid support with vibration isolation. We set

the working distance and the objective distance at 26 cm and 6 m, respectively. The demagnification factors are 9.2 and 35.4 for horizontal and vertical directions, respectively. The focused microbeam is scanned across a target two-dimensionally using an electrostatic beam scanner. The scanner is located downstream of the quadrupole doublet and the maximum scanning area is larger than 1×1 mm^2 for 3 MeV proton beams.

Analysis System Improvements

The target chamber is a rectangular box and is applicable to either in-vacuum or in-air analysis without changing the main body. For multimodal analysis, two X-ray detectors and three charged particle detectors can be mounted simultaneously[6-8]. For 3D μ-CT, an X-ray CCD camera (C8800X; Hamamatsu photonics), a rotating sample stage and a target to produce X-rays are also mounted on this chamber[9-11]. In the present study, further improvements were introduced to the target chamber, as shown in Fig. 1. Two X-ray detectors are attached to both sides of the chamber and are not shown.

For in-vacuum analysis, hydrogen is analyzed using off-axis STIM. In a previous study, a Si-PIN photodiode was used for both off-axis STIM and Direct STIM measurements. Superior energy resolution of the Si-PIN photodiode is efficient for direct STIM measurement[8]. However, the small size of the detector occasionally restricted detection efficiency in hydrogen analyses. For that reason, an ion-implanted Si detector with a larger sensitive area of 50 mm^2 was installed. Detection efficiency of the system is now three times higher than that of the previous system. The scattering angle is 28 degrees, which is sufficient to separate proton peaks that are scattered from hydrogen and from other elements, even in the thickness of 50 μm of organic films.

For the in-air system, on/off axis STIM for simultaneous density mapping with PIXE and RBS is newly available. It will be useful for damage monitoring in biological cell analysis and for correction of X-ray self-absorption in samples. A thin scattering foil (C or Al) is placed ~20 mm downstream of the sample. Scattered protons are detected by a Si-PIN photodiode which is set at 28 degrees with respect to the beam axis. The detector is well collimated to reduce energy broadening by kinematics.

A compact secondary electron detector is newly installed for secondary electron imaging (see Fig. 1). In the previous system, secondary electrons were detected by a plastic scintillator with a photomultiplier. The detector was not compact, and was therefore not able to cooperate with other detector systems. A compact ceramic channel electron

multiplier (CEM, MD-502; Amptek Inc.) is very compact (1.9 cm diameter×3.8 cm long) and is not obstructive to other detector systems.

Microbeam system performance

After the installation, performance of the system was tested by a micro-PIXE analysis for a Cu mesh (1000 lines/inch). The lower limit of the beam spot size was 2 μm, which is much larger than the design value[4]. The main reason for the limitation is parasitic field contamination from microbeam line components. Especially, the tungsten carbide slit chips cause strong field contamination. X-ray maps from Cu mesh (1000 lines/inch) measured with the baffle slit open and with the baffle slit closed are shown in Fig. 2. Although the mesh image was clearly apparent when the baffle slit was opened, the beam was defocused and was shifted when the baffle slit was closed. This is an effect of parasitic field existing at the baffle slit. The baffle slit has no an electric driving mechanism which might cause electric or magnetic fields. Two of the slit chips used in the baffle slit were magnetized strongly and attracted paper clips. The field contamination was therefore ascribed to the tungsten carbide slit chips. This magnetism is caused by cobalt element that is used as a binder in the slit chip. Although the tungsten carbide itself is not magnetized, cobalt shows strong magnetism and is magnetized easily[13]. The slit chip contains about 10% cobalt. The magnetization arises from manufacturing processes and should be eliminated. Finally, the slit chips of the divergence-defining slit and the baffle slit, whose parasitic field strongly affects microbeam formation, were replaced by the other chips whose elemental concentration of cobalt is less than 10% that of previous chips. After replacement of the chips, defocusing and beam shifting do not occur in any slit position.

Effects of parasitic field contamination was measured using the grid-shadow method[5]. In the grid shadow method, the beam is focused on the image plane, where a fine mesh grid is placed, by a single quadrupole lens and casts shadow pattern on a scintillator downstream. The shadow pattern is influenced strongly by lens aberrations and parasitic field contaminations of the microbeam system. In the present study, a Au mesh (2000 lines/inch) was placed on the image plane and a shadow pattern was obtained on a ZnS(Ag) scintillator located 53 mm downstream of the grid. The sensitivity of the grid shadow method is also increased by reducing the angle between the divergence axis of quadrupole and the grid bar. Smaller angles produce fewer grid bar shadows and higher sensitivity, especially for higher order field contamination. In this study, we set the angle as 1.75

degrees. Figure 3 shows theoretical grid shadow patterns with 0–0.2% sextupole field contamination superimposed onto the quadrupole field calculated by the beam optics computer codes, PRAM and OXTRACE[3)], with identical beam conditions. The theoretical shadow pattern shows that the minimum detectable limit corresponds to approximately 0.05% for sextupole field contamination. Figure 4 shows the measured grid shadow patterns for the two quadrupole lenses with a 3 MeV proton beam. The beam is screened by the beam scanner in the divergence plane. Therefore, the number of grid bars is fewer than the theoretical pattern. Although measured shadow patterns in the horizontal focus show slight deformation resulting from sextupole field contamination, shadow patterns in the vertical focus are not deformed. Both lenses show a similar trend. In comparison with the calculated results, sextupole field contamination in the horizontal focusing is estimated as less than 0.1%. Contamination of the skew sextupole field is less than 0.1%. Therefore, it is difficult to observe deformation in the measured pattern, which implies that sextupole field contamination in the horizontal plane (skew sextupole field contamination in the vertical plane) remains. This contamination source might be the lens itself or another part of the microbeam line. One possibility is that the cancellation of excitation current of the quadrupole is not perfect. This lens was designed so that the excitation current from pole to pole is canceled by the return current. However, no cancellation is made in the upper part of the lens where terminals exist. Because the coils consist of only 22 turns, such effects might cause the problem. To reduce the effect of the contamination field, the 1st quadrupole uses horizontal focusing and the 2nd lens uses vertical focusing (divergence-convergence); the scanner is located downstream.

Then, the beam spot size was measured by scanning the beam across mesh samples (Ni and Au mesh, 2000 lines/inch) and measuring X-rays. Horizontal and vertical line profiles were fitted by symmetric double Gaussian convolution and beam spot sizes were obtained. The line profiles were well reproduced using the symmetric double Gaussian convolution, which implies that the beam profile can be assumed to be of Gaussian shape. Figure 5 shows horizontal and vertical beam spot sizes versus object sizes. These measurements were carried out in the same beam divergence of 0.2 mrad which corresponded to our normal divergence in the high-current regime for ion beam analyses. Beam spot sizes diminished concomitant with the object slit sizes and were better than those that were predicted from the calculation. A spot size of 0.4×0.4 μm^2 was obtained at an object size of 30×10 μm^2 with a beam current of several tens of pA. Beam size estimations

using the deconvolution method are strongly dependent on the mesh quality and are sometimes overestimated in the range less than 1 μm because we assume the mesh edges to be very sharp. The cross sections of mesh grid bars are trapezoidal or round to some degree. Therefore, the beam spot size will be better than 0.4×0.4 μm^2. Figure 6 shows secondary electron images of Ni mesh (1000 lines/inch) measured using an electron microscope and the microbeam system with object size of 25×10 μm^2 and beam divergence of 0.2 mrad. The secondary electron image measured using the microbeam system clearly represents the steps of the bars and round shape of the corner, which corresponds to the image obtained using the electron microscope. This fact shows that resolution of better than 0.4 μm is obtained and is consistent with that obtained using deconvolution method. These measurements were carried out with the divergence of 0.2 mrad for the high-current regime. The result of the grid shadow implies that a better beam spot size will be obtained in a low-current regime where the object size and beam divergence are one-tenth lower.

Even in the same beam condition mentioned above, the beam spot size of 1 μm is a lower limit in the actual experimental setup where X-ray detectors, RBS detector, and other detectors are set in a chamber. The grid-shadow method revealed the source of this problem. The grid-shadow patterns in this situation are shown in Fig. 7. Strong sextupole or higher order field contamination are observed. By removing the annular Si surface barrier detector (TC-019-150-100; Ortec) positioned 40 mm upstream of the sample position, field contamination was eliminated. The grid-shadow pattern in Fig. 7 was measured without applying bias voltage to the annular detector. The holder of the annular detector is made of plastic, which adds no field. Therefore, the parasitic field was ascribed to the magnetic field of the annular Si surface barrier detector itself. In fact, the annular detector imparted a field strength of ~10 μT, as measured using a magnetometer. Elements that show strong magnetism are used in the detector body. The RBS detector was replaced by another annular ion-implanted Si detector (ANPD 300-19-100RM; Canberra). The detector gave a weaker magnetic field, which was also measured using a magnetometer. Following change, the field contamination of the system was reduced to a normal level and performance of the microbeam system was improved greatly, even in the actual analysis. Components that must be set near the beam path should have their magnetism eliminated; the grid shadow method is very effective to clarify the source of parasitic field.

Conclusion

A microbeam system was constructed at the Tohoku University Dynamitron laboratory and optimization of the system was undertaken. Minimum beam spot size of the microbeam was limited at 2×2 μm^2 by parasitic field contamination. This parasitic field contamination was ascribed to the tungsten carbide slit chips and the annular Si surface barrier detector in the case of RBS analysis. The parasitic field contamination of the system was greatly reduced by replacing these components, as confirmed by the grid shadow method, and the microbeam system performance was improved. The minimum beam spot size of 0.4×0.4 μm^2 at a beam current of several tens of pA is obtained, which is the optimum expected from the accelerator performance. The results obtained using the grid-shadow method indicate that a beam spot size of less than 0.4 μm is obtainable in the low-current regime.

While improving the microbeam system, simultaneous in-air/in-vacuum PIXE, RBS, SEM, and STIM analyses, in addition to 3D μ-CT, were developed and are now being applied to biological, environmental, and other fields.

Acknowledgements

This study was partly supported by Grants-in-Aid for Scientific Research, (S) No. 13852017, (B) No. 18360450, (C) No. 16560731, and a Grant-in-Aid for Scientific Research in Priority Areas under Grant No. 14048213 from the Ministry of Education, Culture, Sports, Science and Technology, Japan. The authors would like to thank Prof. Jamieson D.N. of the University of Melbourne, for his valuable suggestions and advice in reducing field contamination and introducing the PRAM and OXTRACE computer codes. The authors would like to acknowledge the assistance of Mr. Sakamoto R. R. and Fujisawa M. for maintenance and operation of the Dynamitron accelerator. The authors would like to thank Mr. Komatsu K., Nagaya T. and Akama C. for their assistance in constructing the microbeam and target system.

References

1) Watt F. and Grime G.W., Principal and Applications of High-energy Ion Microbeams, Adam Hilger, Bristol, 1987.
2) Johansson S.A.E., Campbell J.L. and Malmqvist K.G., Particle-Induced X-ray Emission Spectrometry (PIXE), John Wiley and Sons, N.Y., 1995.
3) Breese M.B.H., Jamieson D.N., and King P.J.C., Materials Analysis using Nuclear Microprobe, John Wiley and Sons, N.Y., 1995.

4) Matsuyama S., Ishii K., Yamazaki H., Sakamoto R., Fujisawa M., Amartaivan Ts., Ohishi Y., Rodoriguez M., Suzuki A., Kamiya K., Oikawa M., Arakawa K., and Matsumoto N., Nucl. Instr. and Meth., **B210** (2003) 59.
5) Jamieson D. N. and Legge G. J. F., Nucl. Instr. and Meth. **B29** (1987) 544.
6) Matsuyama S., Ishii K., Yamazaki H., Barbotteau Y., Amartaivan Ts., Izukawa D., Hotta K., Mizuma K., Abe S., Oishi Y., Rodriguez M., Suzuki A., Sakamoto R., Fujisawa M., Kamiya K., Oikawa M., Arakawa K., Imaseki H., and Matsumoto N., Int. J. of PIXE, **14** (1&2) (2004) 1.
7) Matsuyama S., Ishii K., Abe S., Ohtsu H., Yamazaki H., Kikuchi Y., Amartaivan Ts., Inomata K., Watanabe Y., Ishizaki A., Barbotteau Y., Suzuki A., Yamaguchi T., Momose G., and Imaseki H., Int. J. of PIXE, **15** (1&2) (2005) 41.
8) Matsuyama S., Ishii K., Yamazaki H., Kikuchi Y., Amartaivan Ts., Abe S., Inomata K., Watanabe Y., Ishizaki A., Oyama R., Kawamura Y., Suzuki A., Momose G., Yamaguchi T., and Imaseki H., Int. J. of PIXE, **15** (3&4) (2005) 257.
9) Ishii K., Matsuyama S., Yamazaki H., Watanabe Y., Yamaguchi T., Momose G., Amartaivan Ts., Suzuki A., Kikuchi Y., and Galster W., Int. J. of PIXE, **15** (3&4) (2005) 111.
10) Ishii K., Matsuyama S., Yamazaki H., Watanabe Y., Kawamura Y., Yamaguchi T., Momose G., Kikuchi Y., Terakawa A., and Galster W., Nucl. Instr. and Meth. **B249** (2006) 726.
11) Ishii K., Matsuyama S., Watanabe Y., Kawamura Y., Yamaguchi T., Oyama R., Momose G., Ishizaki A., Yamazaki H., and Kikuchi Y., submitted to Nucl. Instr. and Meth. B.
12) Deves G., Matsuyama S., Barbotteau Y., Ishii K., and Ortega R., Rev. of Sci. Instr., **77** (2006) 056102.
13) Penrice T. W., Int. J. of Refractory Metal and Hard Materials, **15** (1997), 113.

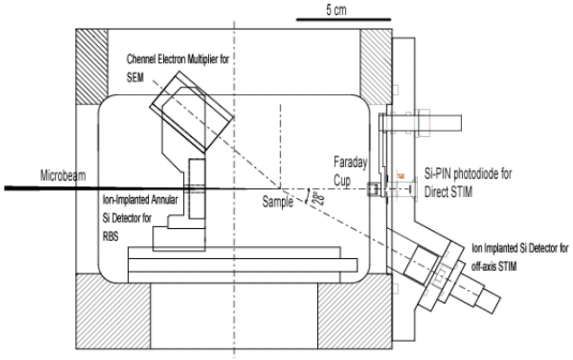

Figure 1. Side cut view of the target chamber.

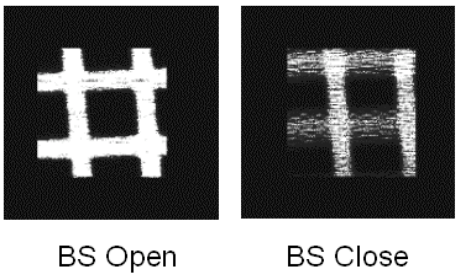

Figure 2. Elemental distribution maps from Cu mesh (1000 lines / inch) measured with the baffle slit open and with the baffle slit closed.

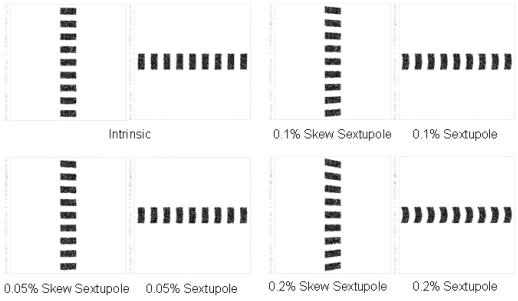

Figure 3. Theoretical grid shadow patterns calculated by PRAM and OXTRACE.

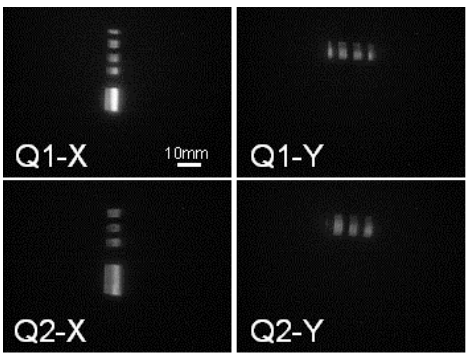

Figure 4. Measured grid shadow patterns of the two quadrupole lenses for vertical (*X*) and horizontal (*Y*) focusing.

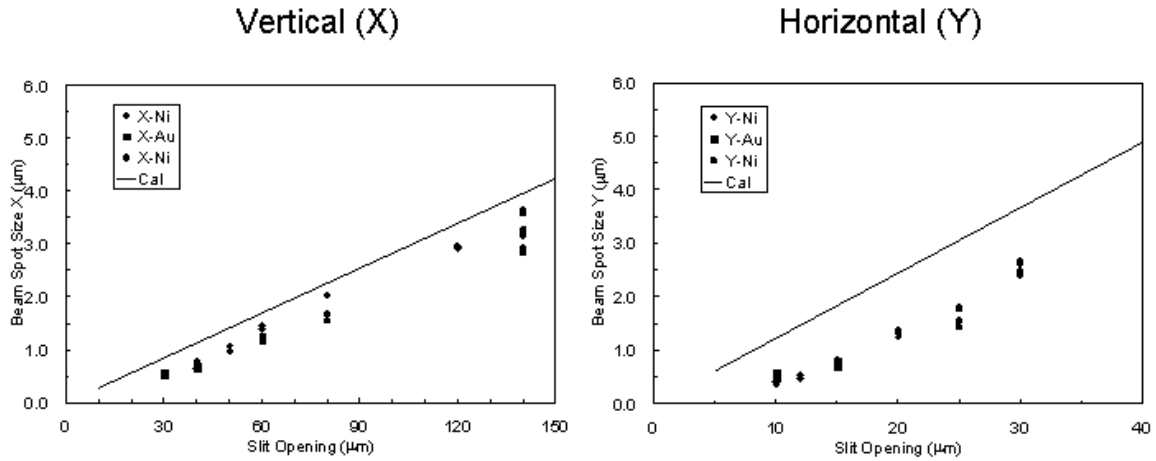

Figure 5. Horizontal and vertical beam spot sizes versus object sizes.

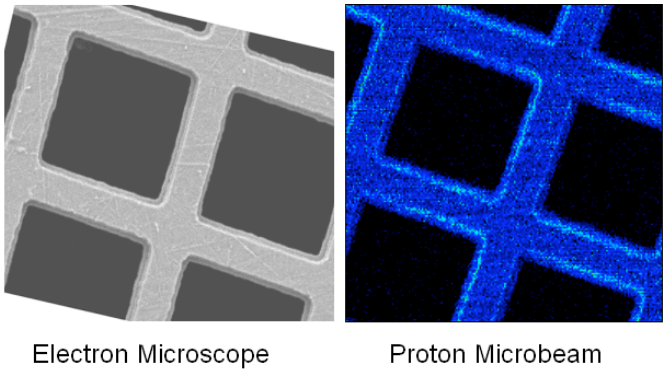

Figure 6. Secondary electron images of Ni mesh (1000 lines/inch) measured using an electron microscope and the microbeam system.

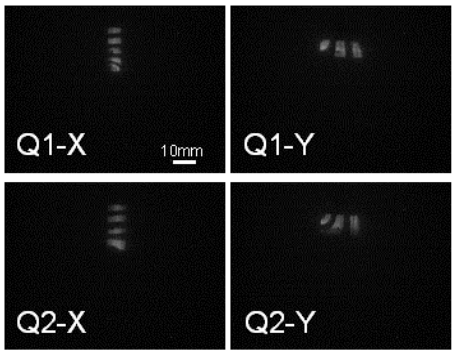

Figure 7. Measured grid shadow patterns with a parasitic field from the annular detector.